

# Mesoscopic Helices of Polar Domains in a Quadruple Perovskite

Yang Zhang,<sup>1,\*</sup> Mingyu Xu,<sup>2</sup> Jie Li,<sup>3</sup> Suk Hyun Sung,<sup>1</sup>  
Sang-Wook Cheong,<sup>4</sup> Weiwei Xie,<sup>2</sup> and Ismail El Baggari<sup>1,†</sup>

<sup>1</sup>*The Rowland Institute at Harvard,*

*Harvard University, Cambridge, MA 02138, USA*

<sup>2</sup>*Department of Chemistry, Michigan State University, East Lansing, MI 48824, USA*

<sup>3</sup>*Department of Earth and Environmental Sciences,*

*University of Michigan Ann Arbor, MI 48109, USA*

<sup>4</sup>*Keck Center for Quantum Magnetism and Department of Physics and Astronomy,  
Rutgers University, New Jersey 08854, USA*

(Dated: June 13, 2025)

## Abstract

A significant effort in condensed matter physics is dedicated to the search for exotic arrangements of electric dipoles. Beyond collinear alignments of electric dipoles, more complex arrangements analogous to magnetic spin textures, such as polar vortices and skyrmions, have been realized. Here we report atomic-scale visualizations of a candidate for helical texture of electric dipoles, the lightly doped quadruple perovskite  $\text{BiCu}_x\text{Mn}_{7-x}\text{O}_{12}$ . Rather than forming a continuous incommensurate helical structure, this material exhibits a mesoscale ordering of ferroelastic and polar domains. Across domains, bismuth's polar displacement rotates discretely following a consistent handedness, giving rise to a mesoscale helical pattern. We observe both right-handed and left-handed chiralities associated with helical ordering. The mesoscopic helices of polar order observed in our work would provide an opportunity to realize emergent chiral-optical activity in ferroelectric crystals akin to supramolecular assemblies.

---

\* yzhang6@fas.harvard.edu

† ielbaggari@fas.harvard.edu

Spin arrangements in magnets underlie diverse functional properties. The simplest configurations involves aligned (ferromagnet) or anti-aligned (antiferromagnet) spins, but these can also break into complex domain patterns [1, 2]. Magnetic systems are a fertile ground for realizing much more exotic non-collinear spin textures, such as cycloids, helicoids, or skyrmions [3, 4]. Such exotic spin spirals have emerged as an integral part to realizing multiferroic functionality that couples electrical, magnetic, and structural degrees of freedom. For example, cycloidal spirals of spins,  $\mathbf{S}_i$ , can lead to polarization,  $\mathbf{P}$ , given by  $\mathbf{P} \sim \mathbf{r}_{ij} \times [\mathbf{S}_i \times \mathbf{S}_j]$  and where  $\mathbf{r}_{ij}$  is the vector connecting  $\mathbf{S}_i$  and  $\mathbf{S}_j$ . Canonical examples of spin spirals include  $\text{TbMnO}_3$ ,  $\text{Ni}_3\text{V}_2\text{O}_6$ , and  $\text{MnWO}_4$  [5–10].

Electrical dipoles can also form aligned (ferroelectric) or anti-aligned order (antiferroelectric), as well as complex domain configurations [11–14]. While it is generally difficult to realize exotic electric dipole textures, advances in heterostructure-engineering have enabled the creation of emergent topological structures like polar vortices and merons in  $\text{PbTiO}_3/\text{SrTiO}_3$  superlattices [15–19]. These textures are achieved by carefully balancing the competition between strain, electrostatics, and polar instabilities [20, 21]. However, the complexity of fine tuning these interactions motivates a parallel effort to discover bulk materials that can intrinsically host complex textures of electric dipoles, which could in turn inform new design principles for intricate ferroic states.

$\text{BiMn}_7\text{O}_{12}$  is a so-called quadruple perovskite, where the Bi is 12-fold-coordinated and Mn occupies two distinct coordination sites: one in square-planar-coordination and another in octahedral coordination similar to perovskites (Fig. 1A). With Bi and Mn in the chemical formula, the compound has two ingredients that drive electronic instabilities: (i) the  $\text{Mn}^{3+} 3d_{eg}$  electrons and (ii) the  $6s^2$  lone pair of  $\text{Bi}^{3+}$  [22, 23]. The former promotes orbital order and associated Jahn-Teller distortions, while the latter promotes polar displacements of Bi and associated local electric dipoles.  $\text{BiMn}_7\text{O}_{12}$  forms a cubic  $Im\bar{3}$  parent structure above 610 K and undergoes a proper ferroelastic phase transition to a monoclinic structure with  $C2/m$  space group down to  $\sim 460$  K [24]. At low temperature,  $\text{BiMn}_7\text{O}_{12}$  hosts two low-symmetry polar phase transitions, a  $Cm$  phase below  $\sim 390$  K and a  $P1$  phase at room temperature. The latter is attributed to polar displacements of the Bi cations which align close to the  $[1\bar{1}0]_{pc}$  direction with a subtle rotation around  $[001]_{pc}$  axis (right panel of Fig. 1A, all crystallographic axes in the polar phase are based on the pseudocubic system) [24, 25]. In addition, the system exhibits two, and possibly three, antiferromagnetic phase transitions



below 59 K, involving ordering of the distinct Mn sublattices [26]. With ferroelectricity experimentally demonstrated,  $\text{BiMn}_7\text{O}_{12}$  is a prime candidate to realize novel multiferroic states [27, 28].

After light hole doping through copper substitution, a combined X-ray and neutron study has proposed two novel low-temperature phase transitions in  $\text{BiCu}_{0.1}\text{Mn}_{6.9}\text{O}_{12}$  that radically differ from those in the parent  $\text{BiMn}_7\text{O}_{12}$  compound [29]. Instead of the usual phase transitions, the system hosts two incommensurately modulated phases, characterized by strong incommensurate satellite reflections in reciprocal space. Structural refinements using superspace groups have proposed a long-sought helical dipole wave, featuring continuous rotation of Bi atomic displacements in a helical pattern, which defines an axial vector along the pseudocubic  $[111]_{pc}$  direction (Fig. 1B). According to the refined atomic positions, the helical bismuth atomic modulations appear notably large, reaching up to 0.4 Å in amplitude. Such helical dipole modulation may be viewed as a realization of structural chirality in ferroelectric crystals, which, in analogy to spin-spiral-driven multiferroicity, could open possibilities for coupling structural axial vectors and ferroelectricity.

Here we utilize scanning transmission electron microscopy (STEM) to map the real-space structure of the room-temperature dipolar phase of  $\text{BiCu}_{0.1}\text{Mn}_{6.9}\text{O}_{12}$ . Direct imaging shows no evidence of an incommensurate helical modulation in the positions of Bi atoms. Instead, light copper doping introduces a high density of structural domains throughout the crystal. These domains are ferroelastic, aligning in the  $(\bar{1}\bar{1}1)_{pc}$  plane and each one sets a distinct direction of the Bi polar displacement. Remarkably, we uncover a new form of long-range helical order - not in the atomic displacements themselves, but in the arrangement of domain configurations. As one crosses from one domain to the next, the direction of polar displacement rotates clockwise (or counterclockwise) around the  $[\bar{1}\bar{1}1]_{pc}$  axis, creating a mesoscopic helical pattern of polar rotation. This behavior reveals a striking emergent self-organization, involving a helical ordering of polar domains on the mesoscale.

The incorporation of copper and its concentration was first confirmed through refinement of X-ray diffraction and energy dispersive X-ray spectroscopy (see Tables S1-S4 and Fig. S1). Figure 1C shows simulated high-angle annular dark field STEM (HAADF-STEM) images of  $\text{BiCu}_{0.1}\text{Mn}_{6.9}\text{O}_{12}$  viewed along  $[11\bar{2}]_{pc}$  zone axis. In the HAADF-STEM imaging mode, electrons that have scattered to high angles are collected and so the image intensity scales monotonically with the atomic number. Bi atomic columns appear brighter than Mn, while

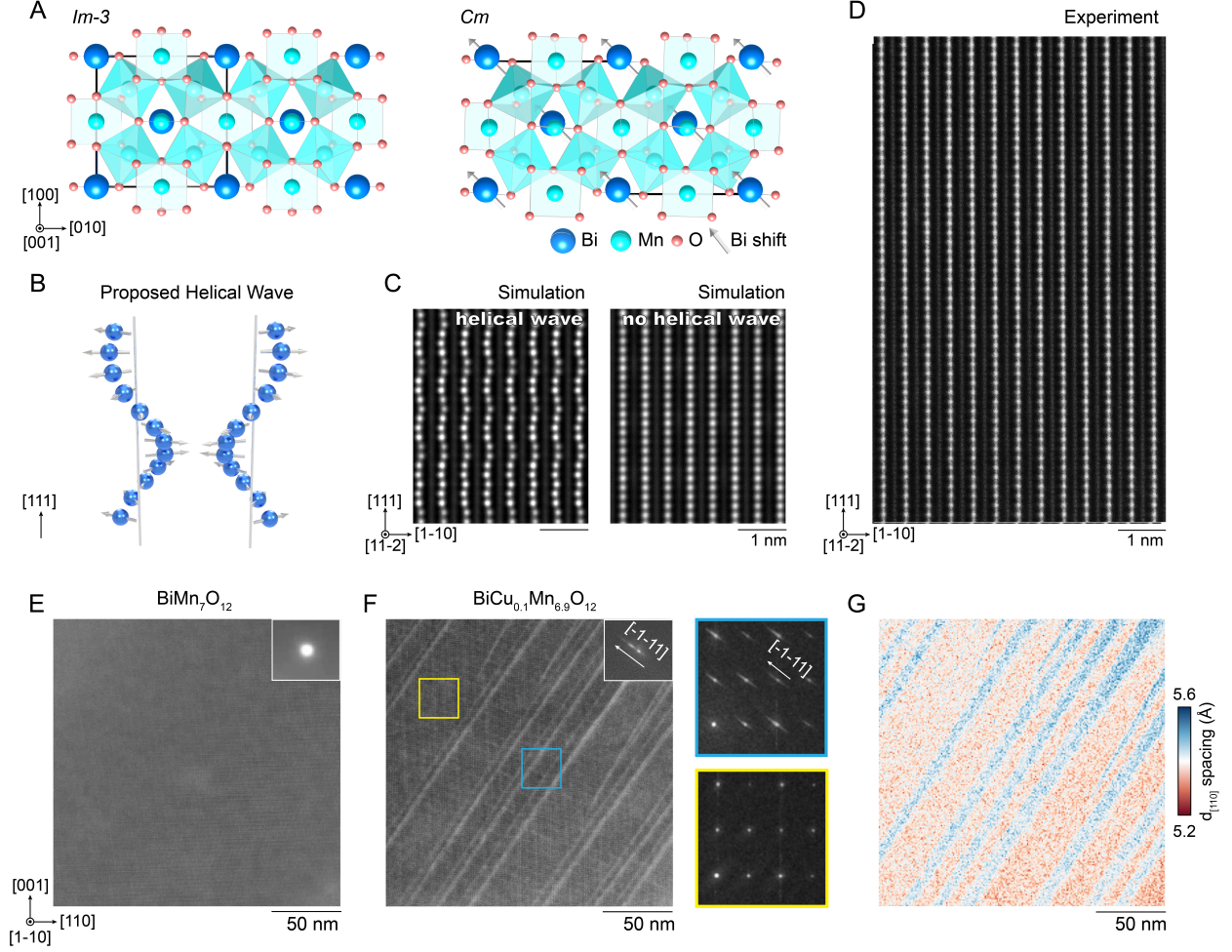


FIG. 1. **Emergence of ferroelastic domains with copper doping.** (A) Atomic structure of  $\text{BiMn}_7\text{O}_{12}$  in the  $Im\bar{3}$  (left panel) and  $Cm$  (right panel) phase. The gray arrow in  $Cm$  phase shows the polar displacement of Bi along  $[1\bar{1}0]_{pc}$ . All crystallography indexing are based on the pseudocubic lattice. (B) Previously proposed incommensurate dipole helical wave in  $\text{BiCu}_{0.1}\text{Mn}_{6.9}\text{O}_{12}$ . Left and right-handed chiralities are shown. (C) Simulated ADF-STEM image of structures with (left panel) and without (right panel) dipole helical wave. The projection is along  $[11\bar{2}]_{pc}$  (D) Experimental ADF-STEM of  $\text{BiCu}_{0.1}\text{Mn}_{6.9}\text{O}_{12}$  along  $[11\bar{2}]_{pc}$  shows no helical Bi modulation. (E, F)  $250 \times 250 \text{ nm}^2$  field-of-view LAADF-STEM image of (E)  $\text{BiMn}_7\text{O}_{12}$  and (F)  $\text{BiCu}_{0.1}\text{Mn}_{6.9}\text{O}_{12}$ , revealing the presence of high density of domain boundaries in the latter. Inserts are the  $(114)_{pc}$  Bragg peak. An incommensurate peak along the  $[\bar{1}\bar{1}1]_{pc}$  direction is evident only in the doped system. The right panel of (F) is the Fourier transform from regions highlighted by yellow and blue rectangles. The incommensurate peak is absent without a domain boundary (lower panel). (G) Lattice spacing along  $[110]_{pc}$  in  $\text{BiCu}_{0.1}\text{Mn}_{6.9}\text{O}_{12}$  measured by 4D-STEM (see SI for more details). The field-of view is same as (F).

O columns are not visible due to their low scattering cross section. The proposed helical pattern of Bi atoms will give a strong modulation on Bi positions along the  $[111]_{pc}$  direction, which should be prominently visible in ADF-STEM image when view along  $[11\bar{2}]_{pc}$  axis (left panel of Fig. 1C). However, the experimental atomic-resolution data (Fig. 1D) does not reveal modulated bismuth positions; instead, the structure matches that of the undoped parent material (right panel of Fig. 1C), showing an unexpected divergence from the refined atomic structure.

Stark differences between the undoped and Cu-doped samples, however, become evident at mesoscopic length scales. Figures 1E and F display  $250 \times 250 \text{ nm}^2$  low-angle ADF STEM (LAADF-STEM) images of both samples along  $[\bar{1}\bar{1}0]$  axis. The LAADF scattering signal includes electrons that have scattered to low angles and is more sensitive to lattice strain and structural defects, leading to enhanced contrast [30, 31]. As shown in Figs. 1E and F, a high density of bright lines appears across the field-of view in  $\text{BiCu}_{0.1}\text{Mn}_{6.9}\text{O}_{12}$ , a feature consistently observed in multiple samples (Fig. S2). In comparison, the undoped sample exhibits either a complete absence of such line contrasts or a much lower density over similar fields of view (Fig. S3). The lines are oriented perpendicular to the  $[\bar{1}\bar{1}1]_{pc}$  direction, matching the direction of incommensurate superlattice peaks (inset of Figs. 1E and F, raw data shown in Fig. S4). A detailed analysis of the superlattice peaks reveals that the incommensurate peaks, previously attributed to a helical displacive modulation of Bi atoms, relate instead to the domain boundaries. Regions lacking domains show no incommensurate peaks, whereas regions with line features consistently exhibit them (right panel of Fig. 1F). Quantitative analysis based on 4D-STEM (see Methods for details) reveals that all of these line contrasts correspond to boundaries between ferroelastic domains, across which the lattice spacings along  $[001]_{pc}$  and  $[110]_{pc}$ , as well as the crystallographic angles, undergo distinct changes (Fig. 1G and Fig. S5).

Typically, an incommensurate superlattice peak in diffraction indicates the presence of a real-space modulation whose periodicity is not an integer multiple of the underlying unit cell. Three-dimensional translational periodicity is broken, and structural refinements must use higher-dimensional superspace groups. However, the solution space for incommensurate structures is highly degenerate, making structure determination particularly challenging. This complexity is exacerbated by the presence of real-space features within the crystal. Notably, incommensurate superlattice peaks may reflect localized features in a crystal, such

as discommensurations seen in charge order systems [32–34]. In our case, sharp domain boundaries in the crystal create intense superlattice reflections that are incommensurate with the lattice periodicity. Summarizing thus far, our results indicate that  $\text{BiCu}_{0.1}\text{Mn}_{6.9}\text{O}_{12}$  preserves the underlying crystallographic structure of  $\text{BiCuMn}_7\text{O}_{12}$ , and that the primary effect of copper doping is the substantial increase in the density of structural domains.

As these domains are ferroelastic, we next explore their interplay with polar Bi displacements. In the pseudocubic cell, there are three (or six if distinguish positive and negative directions) inequivalent  $\langle 110 \rangle_{pc}$  orientations lying on the  $(\bar{1}\bar{1}1)_{pc}$  pseudocubic plane (labeled I, II and III in Fig. 2A). By precisely fitting and mapping atomic positions using HAADF-STEM along  $[1\bar{1}0]_{pc}$  axis (Fig. 2B), we extract (i) local bond distances,  $d_{[110]_{pc}}$  and (ii) polar displacement of Bi atoms relative to the Mn sublattice,  $\Delta_{\text{Bi}}$ , as defined in the right panel of Fig. 2B. Figure 2C shows differences in  $d_{[110]_{pc}}$  when polar displacements are along three inequivalent  $\langle 110 \rangle_{pc}$  orientations, revealing ferroelastic domains. Type-I domain is evident due to its larger  $d_{[110]_{pc}}$  of 5.47 Å. Type-II and III domains have a smaller  $d_{[110]_{pc}}$ , but we cannot be reliably distinguish between them since in projection they have similar lattice constants and are close to the precision limit of atomic fitting.

Unlike the lattice constants, polar displacements of Bi have characteristic signatures that uniquely determine all ferroelastic domain variants. Although STEM is a projection imaging technique, the chosen viewing direction identifies a distinct in-plane component of the polar displacement for each of the domains. As shown in the atomic model (Fig. 2C) and experimental measurement (Fig. 2D), Type-II and Type-III domains exhibit a significant yet distinct in-plane components of  $\Delta_{\text{Bi}}$ , identifiable through finite amplitude and distinct directions.  $\Delta_{\text{Bi}}$  in Type-I domains is largely along the imaging direction, yet it still has a measurable, albeit smaller, in-plane component. Figure 2E shows polar histograms of  $\Delta_{\text{Bi}}$ , revealing that each of the three types of polar domains has a characteristic amplitude and angle of the in-plane projection of the displacement. Detailed multislice simulations (see Methods and Fig. S6) provide additional confirmation of the accurate identification of the three polar domains.

Figure 2F shows a map of  $d_{[110]_{pc}}$  from  $50 \times 35 \text{ nm}^2$  region, which spans multiple domains (also see Fig. S7). Figure 2G shows a  $\Delta_{\text{Bi}}$  map from the same region, with the color and transparency reflecting the direction and amplitude, respectively. While only two domains are visible in the  $d_{[110]_{pc}}$  map, the  $\Delta_{\text{Bi}}$  unearths all three domains. Further inspection of

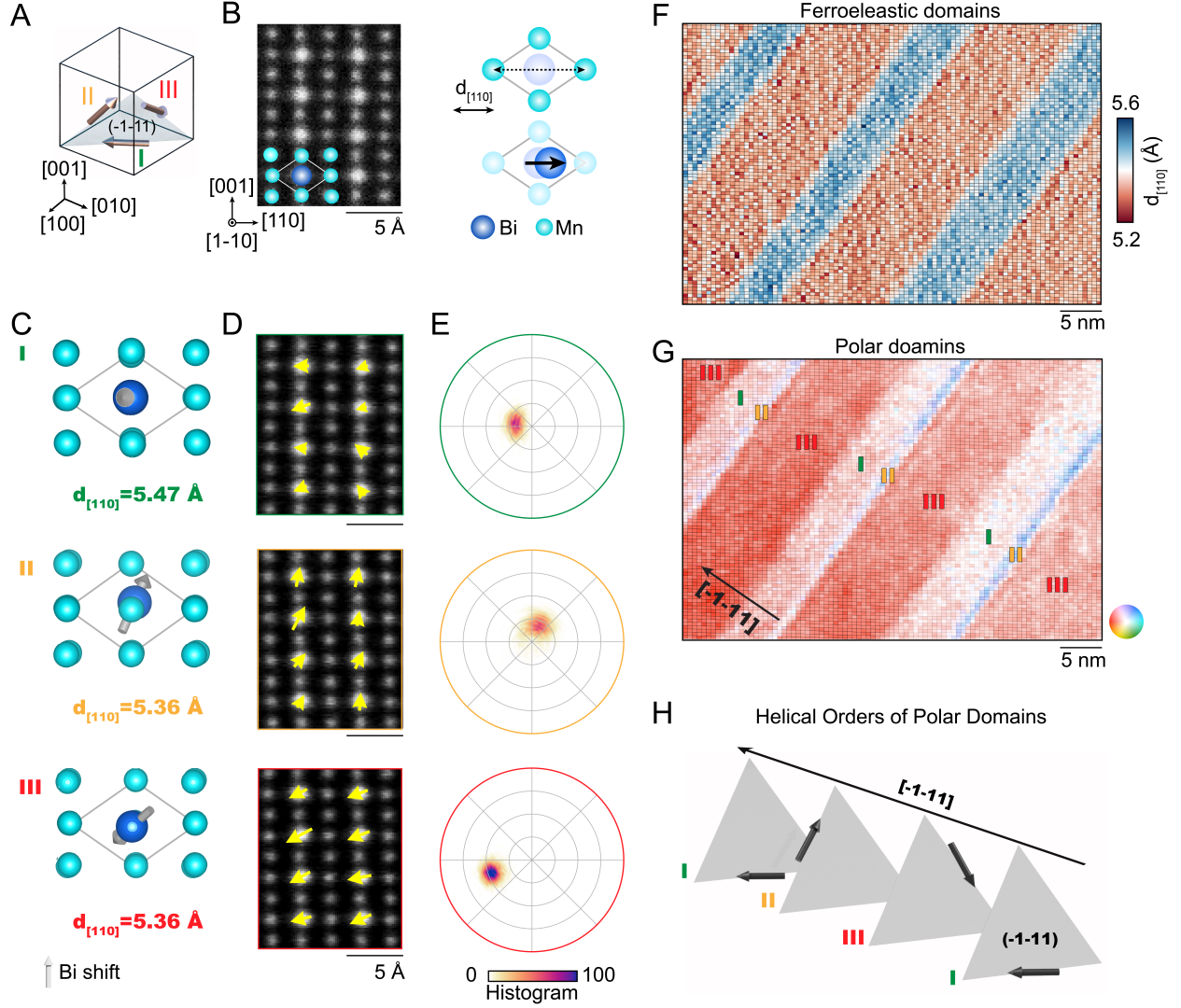


FIG. 2. **A mesoscopic helix of polar domains.** (A) Schematic graph of three distinct  $\langle 110 \rangle_{pc}$  polar displacements lying on the  $(\bar{1}\bar{1}1)_{pc}$  plane, corresponding to the three ferroelastic domains (I, II and III). (B) HAADF-STEM image of  $\text{BiCu}_{0.1}\text{Mn}_{6.9}\text{O}_{12}$  viewed along  $[1\bar{1}0]_{pc}$ . Right panel is the definition of projected lattice spacing along  $[110]$  ( $d_{[110]_{pc}}$ ) and Bi polar displacement ( $\Delta_{\text{Bi}}$ ) measured in experiment. (C) Atomic structures viewed along  $[1\bar{1}0]_{pc}$  directions in three ferroelastic domains (I, II and III). The gray arrow shows  $\Delta_{\text{Bi}}$ . The measured  $d_{[110]_{pc}}$  is at the bottom. (D) HAADF-STEM image overlaid with measured  $\Delta_{\text{Bi}}$  in three ferroelastic domains. (E) Polar histogram of  $\Delta_{\text{Bi}}$  in three ferroelastic domains (I, II and III). The radius of the histogram 40 pm. Each polar displacement vector has unique planar projection. (F)  $d_{[110]_{pc}}$  from  $50 \times 35 \text{ nm}^2$  field-of-view HAADF-STEM image. (G) Projected  $\Delta_{\text{Bi}}$  measured from same field-of-view HAADF-STEM image as (F). The color and transparency represent the polar direction and amplitude, respectively. (H) Schematic representation of ordering of polar domains.

Fig. 2G shows a remarkable result. The sequence of domains follows a repeating "III-II-I" pattern along  $[\bar{1}\bar{1}1]_{pc}$  direction. In three dimensions, this corresponds to a helical self-organization of polar domains over mesoscopic length scales (Fig. 2H). Across each domain boundary along  $[\bar{1}\bar{1}1]_{pc}$  direction, the polar displacement undergoes a 120-degree counterclockwise rotation within the  $(\bar{1}\bar{1}1)_{pc}$  plane. Here, the sense of rotation is defined when viewed along  $[\bar{1}\bar{1}1]_{pc}$ . This produces an asymmetry within the Type-I domains: on one side, they are always preceded by a Type-II domain and, on the other, followed by a Type-III domain. These arrangements extend over hundreds of nanometers and are consistently observed across multiple samples and regions (Fig. S8), indicating a long-range mesoscale helical ordering of polar domains. Such a helical state is an unusual realization of structural chirality, manifesting in this case as a left-handed variant along  $[\bar{1}\bar{1}1]_{pc}$  direction. This mesoscopic helix of polar domains is chiral because it is not superimposable on its mirror image.

An obvious question to ask is whether such polar domains can form a helical ordering with the opposite chirality, as shown in Fig. 3A. Upon conducting additional searches, we discovered the presence of opposite right-handed chirality in the polar domain ordering. Figure 3B shows a 4D-STEM map of polarization (see Methods and Figs. S9-S11), further processed with difference of Gaussians to better visualize the three domains and their consistent helical arrangement over large scales. Long-range helical orderings with opposite chirality are observed: the color sequence in the right panel is reversed when compared to the left-handed counterpart shown in the left panel. Further atomic-scale mapping of a sub-region (Fig. 3C) reveals helical order which involves a clockwise rotation of polar order across domains. This clockwise (right-handed chiral) ordering comprises polar displacements that are  $180^\circ$  reversed relative to the counterclockwise (left-handed chiral) ordering, as seen in the polar histogram in Fig. 3D. These real-space observations thus establish both chiral states of mesoscopic ordering of polar domains.

In ferroelectric materials, electrostatic and elastic energy considerations drive the formation of polar domain configurations that minimize the system's total energy. In this study, we report the discovery of a novel form of emergent ordering in a bulk crystal, characterized by a long-range helical arrangement of polar domains. This mesoscale helical arrangement imparts chirality to the material, with both left- and right-handed variants observed, mimicking those observed in liquid crystals and supramolecular structures [35–37]. Mesoscale



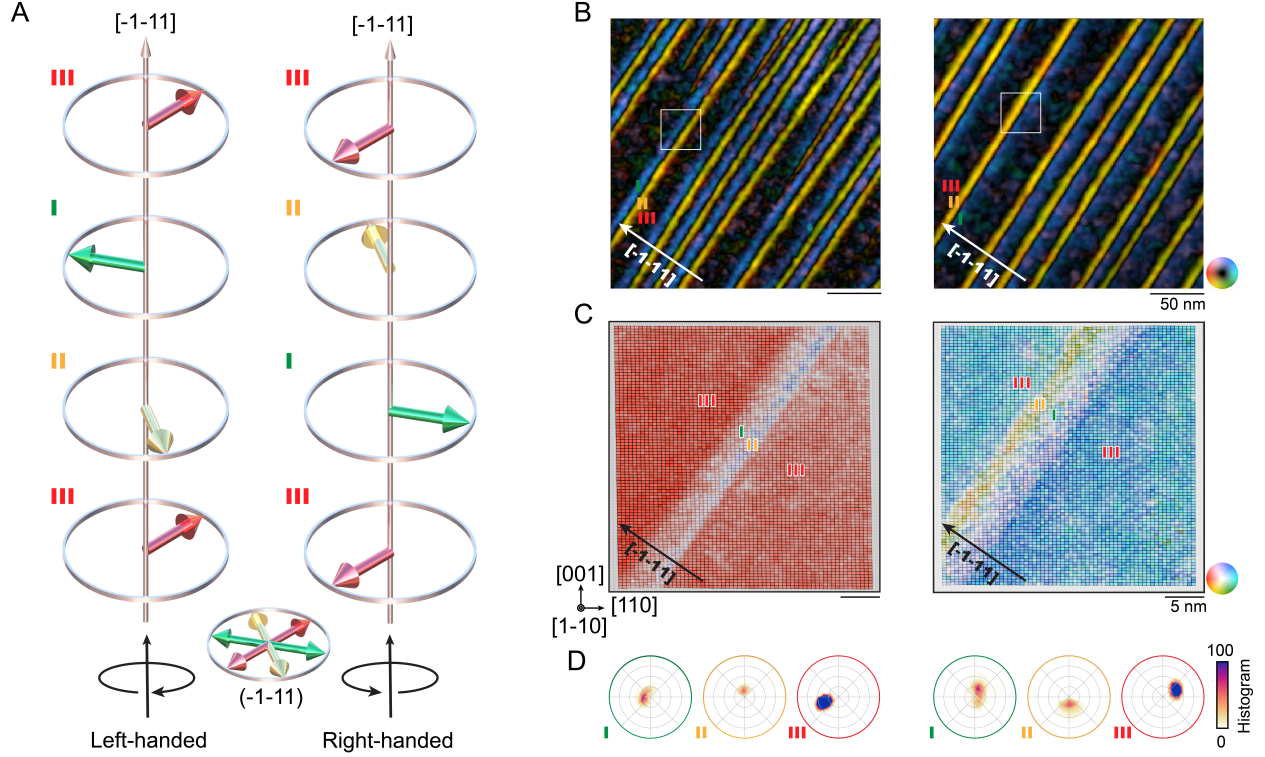


FIG. 3. **Left- and right-handed chirality of mesoscale polar domains.** (A) Schematic graph shows left-handed and right-handed chirality, coupled to helical order of polar domains. (B) Difference of Gaussian applied to large scale 4D-STEM map of polarization reveals long-range repeat of right- (left panel) and left-handed (right panel) helical ordering of polar domains. Domains I (green), II (yellow) and III (red) are labeled. (C) Atomic-scale mapping of polar displacement of sub-regions regions highlighted by white rectangles in (A). (D) Polar histograms of displacements collected from each domain. The radius of the histogram is 40 pm.

features—such as domains and domain walls—often play a key role in enhancing the material’s functionalities [38–41]. Therefore, the emergence of helical domain configurations in  $\text{BiCu}_x\text{Mn}_{7-x}\text{O}_{12}$  provides a new opportunity for engineering chiral textures through mesoscopic ordering of polar building blocks.

To that end, a remarkable finding from this atomic-resolution study is how light copper doping dramatically tunes the density of mesoscopic domains. While the precise mechanism by which copper modulates the domain density remains an open question, the dramatic effect herein presents an opportunity to tune the density of mesoscopic textures such as helical polar textures in the quadruple perovskite. A comprehensive doping study has shown

that copper doping levels up to  $x=1.2$  are linked to a multitude of macroscopic properties including a re-entrant high-temperature phase with near-zero thermal expansion [42, 43]. If our visualizations are any indication, the rich phase diagram of  $\text{BiCu}_x\text{Mn}_{7-x}\text{O}_{12}$  could reflect a range of mesoscopic domain configurations, suggesting a potential to tailor macroscopic responses through domain engineering of bulk crystals. Finally, these results highlight the power of atomic-resolution imaging in uncovering the precise structure of ordered phases.

## ACKNOWLEDGMENTS

We acknowledge discussions with Yu-Tsun Shao, Chuqiao Shi, Xinyan Li, Robert Hovden, Rose Hosking, Andrew W. Murry, Michele Conroy, John Heron, Pu Yu, Houbing Huang and Bo Wang. **Funding:** Y. Z., S. H. S and I. E were supported by the Rowland Institute at Harvard. The high-pressure synthesis and characterization at MSU and University of Michigan were supported by NSF-DMR-2422361 and NSF-DMR-2422362, respectively. Focused ion beam sample preparation was performed at the Harvard University Center for Nanoscale Systems (CNS); a member of the National Nanotechnology Coordinated Infrastructure Network (NNCI), which is supported by the National Science Foundation under NSF award no. ECCS-2025158. S.-W. C. was supported by the W. M. Keck foundation grant to the Keck Center for Quantum Magnetism at Rutgers University. Transmission electron microscopy was carried out through the use of MIT.nano facilities. **Author contributions** Y. Z., I.E. and S.-W. C. conceived the project. Y. Z. and I.E. performed electron microscopy and data analysis with the help of S. S; M. X., J. L., S.-W. C. and W. X. synthesized samples; M. X., J. L. and W. X. performed X-ray diffraction and SEM measurements; Y. Z. and I. E. wrote the manuscript with input from all authors; **Competing interests:** Authors declare no competing interests; **Data and materials availability:** All data are available in the manuscript or the supplementary materials

- 
- [1] C. G. Shull and J. S. Smart, Detection of antiferromagnetism by neutron diffraction, *Physical Review* **76**, 1256 (1949).
  - [2] O. Shpyrko, E. Isaacs, J. Logan, Y. Feng, G. Aeppli, R. Jaramillo, H. Kim, T. Rosenbaum, P. Zschack, M. Sprung, *et al.*, Direct measurement of antiferromagnetic domain fluctuations,



- Nature **447**, 68 (2007).
- [3] X. Yu, Y. Onose, N. Kanazawa, J. H. Park, J. Han, Y. Matsui, N. Nagaosa, and Y. Tokura, Real-space observation of a two-dimensional skyrmion crystal, Nature **465**, 901 (2010).
  - [4] F. Zheng, N. S. Kiselev, F. N. Rybakov, L. Yang, W. Shi, S. Blügel, and R. E. Dunin-Borkowski, Hopfion rings in a cubic chiral magnet, Nature **623**, 718 (2023).
  - [5] T. Kimura, T. Goto, H. Shintani, K. Ishizaka, T.-h. Arima, and Y. Tokura, Magnetic control of ferroelectric polarization, nature **426**, 55 (2003).
  - [6] M. Kenzelmann, A. B. Harris, S. Jonas, C. Broholm, J. Schefer, S. Kim, C. Zhang, . f. S.-W. Cheong, O. P. Vajk, and J. W. Lynn, Magnetic inversion symmetry breaking and ferroelectricity in TbMnO<sub>3</sub>, Physical Review Letters **95**, 087206 (2005).
  - [7] H. Katsura, N. Nagaosa, and A. V. Balatsky, Spin current and magnetoelectric effect in noncollinear magnets, Physical review letters **95**, 057205 (2005).
  - [8] M. Mostovoy, Ferroelectricity in spiral magnets, Physical Review letters **96**, 067601 (2006).
  - [9] N. A. Spaldin and R. Ramesh, Advances in magnetoelectric multiferroics, Nature Materials **18**, 203 (2019).
  - [10] R. Masuda, Y. Kaneko, Y. Tokura, and Y. Takahashi, Electric field control of natural optical activity in a multiferroic helimagnet, Science **372**, 496 (2021).
  - [11] E. Sawaguchi, H. Maniwa, and S. Hoshino, Antiferroelectric structure of lead zirconate, Physical review **83**, 1078 (1951).
  - [12] W. J. Merz, Domain formation and domain wall motions in ferroelectric batio 3 single crystals, Physical Review **95**, 690 (1954).
  - [13] B. B. Van Aken, J.-P. Rivera, H. Schmid, and M. Fiebig, Observation of ferrotoroidic domains, Nature **449**, 702 (2007).
  - [14] C.-L. Jia, K. W. Urban, M. Alexe, D. Hesse, and I. Vrejoiu, Direct observation of continuous electric dipole rotation in flux-closure domains in ferroelectric Pb(Zr,Ti)O<sub>3</sub>, Science **331**, 1420 (2011).
  - [15] A. Yadav, C. Nelson, S. Hsu, Z. Hong, J. Clarkson, C. Schlepütz, A. Damodaran, P. Shafer, E. Arenholz, L. Dedon, *et al.*, Observation of polar vortices in oxide superlattices, Nature **530**, 198 (2016).
  - [16] S. Das, Y. Tang, Z. Hong, M. Gonçalves, M. McCarter, C. Klewe, K. Nguyen, F. Gómez-Ortiz, P. Shafer, E. Arenholz, *et al.*, Observation of room-temperature polar skyrmions, Nature **568**,

- 368 (2019).
- [17] Y. Wang, Y. Feng, Y. Zhu, Y. Tang, L. Yang, M. Zou, W. Geng, M. Han, X. Guo, B. Wu, *et al.*, Polar meron lattice in strained oxide ferroelectrics, *Nature Materials* **19**, 881 (2020).
  - [18] Y.-T. Shao, S. Das, Z. Hong, R. Xu, S. Chandrika, F. Gómez-Ortiz, P. García-Fernández, L.-Q. Chen, H. Y. Hwang, J. Junquera, *et al.*, Emergent chirality in a polar meron to skyrmion phase transition, *Nature Communications* **14**, 1355 (2023).
  - [19] Y. Hu, J. Yang, and S. Liu, Giant piezoelectric effects of topological structures in stretched ferroelectric membranes, *Physical Review Letters* **133**, 046802 (2024).
  - [20] Z. Hong, A. R. Damodaran, F. Xue, S.-L. Hsu, J. Britson, A. K. Yadav, C. T. Nelson, J.-J. Wang, J. F. Scott, L. W. Martin, *et al.*, Stability of polar vortex lattice in ferroelectric superlattices, *Nano letters* **17**, 2246 (2017).
  - [21] J. Junquera, Y. Nahas, S. Prokhorenko, L. Bellaiche, J. Íñiguez, D. G. Schlom, L.-Q. Chen, S. Salahuddin, D. A. Muller, L. W. Martin, *et al.*, Topological phases in polar oxide nanostructures, *Reviews of Modern Physics* **95**, 025001 (2023).
  - [22] W. A. Sławiński, H. Okamoto, and H. Fjellvåg, Triclinic crystal structure distortion of multiferroic BiMn7O12, *Structural Science* **73**, 313 (2017).
  - [23] A. A. Belik, Y. Matsushita, Y. Kumagai, Y. Katsuya, M. Tanaka, S. Y. Stefanovich, B. I. Lazoryak, F. Oba, and K. Yamaura, Complex structural behavior of BiMn7O12 quadruple perovskite, *Inorganic Chemistry* **56**, 12272 (2017).
  - [24] A. Maia, M. Kempa, V. Bovtun, R. Vilarinho, C. Kadlec, J. Agostinho Moreira, A. Belik, P. Proschek, and S. Kamba, Two displacive ferroelectric phase transitions in multiferroic quadruple perovskite BiMn7O12, *Physical Review B* **109**, 134111 (2024).
  - [25] I. S. Soboleva, V. I. Nitsenko, A. V. Sobolev, M. N. Smirnova, A. A. Belik, and I. A. Presniakov, Understanding Complex Interplay among Different Instabilities in Multiferroic BiMn7O12 Using  $^{57}\text{Fe}$  Probe Mössbauer Spectroscopy, *International Journal of Molecular Sciences* **25**, 1437 (2024).
  - [26] D. Behr, A. A. Belik, D. D. Khalyavin, and R. D. Johnson, BiMn7O12: Polar antiferromagnetism by inverse exchange striction, *Physical Review B* **107**, L140402 (2023).
  - [27] F. Mezzadri, G. Calestani, M. Calicchio, E. Gilioli, F. Bolzoni, R. Cabassi, M. Marezio, and A. Migliori, Synthesis and characterization of multiferroic BiMn7O12, *Physical Review B—Condensed Matter and Materials Physics* **79**, 100106 (2009).

- [28] L. Zhou, J. Dai, Y. Chai, H. Zhang, S. Dong, H. Cao, S. Calder, Y. Yin, X. Wang, X. Shen, *et al.*, Realization of large electric polarization and strong magnetoelectric coupling in BiMn<sub>3</sub>Cr<sub>4</sub>O<sub>12</sub>, *Advanced Materials* **29**, 1703435 (2017).
- [29] D. D. Khalyavin, R. D. Johnson, F. Orlandi, P. G. Radaelli, P. Manuel, and A. A. Belik, Emergent helical texture of electric dipoles, *Science* **369**, 680 (2020).
- [30] D. A. Muller, N. Nakagawa, A. Ohtomo, J. L. Grazul, and H. Y. Hwang, Atomic-scale imaging of nanoengineered oxygen vacancy profiles in SrTiO<sub>3</sub>, *Nature* **430**, 657 (2004).
- [31] D. Lee, B. Chung, Y. Shi, G.-Y. Kim, N. Campbell, F. Xue, K. Song, S.-Y. Choi, J. Podkaminer, T. Kim, *et al.*, Isostructural metal-insulator transition in VO<sub>2</sub>, *Science* **362**, 1037 (2018).
- [32] A. Mesaros, K. Fujita, S. D. Eddins, M. H. Hamidian, H. Eisaki, S.-i. Uchida, J. S. Davis, M. J. Lawler, and E.-A. Kim, Commensurate 4a<sub>0</sub>-period charge density modulations throughout the Bi<sub>2</sub>Sr<sub>2</sub>CaCu<sub>2</sub>O<sub>8+x</sub> pseudogap regime, *Proceedings of the National Academy of Sciences* **113**, 12661 (2016).
- [33] I. El Baggari, B. H. Savitzky, A. S. Admasu, J. Kim, S.-W. Cheong, R. Hovden, and L. F. Kourkoutis, Nature and evolution of incommensurate charge order in manganites visualized with cryogenic scanning transmission electron microscopy, *Proceedings of the National Academy of Sciences* **115**, 1445 (2018).
- [34] N. Schnitzer, B. H. Goodge, G. Powers, J. Kim, S.-W. Cheong, I. El Baggari, and L. F. Kourkoutis, Atomic-scale tracking of topological defect motion and incommensurate charge order melting, *Physical Review X* **15**, 011007 (2025).
- [35] N. P. Huck, W. F. Jager, B. De Lange, and B. L. Feringa, Dynamic control and amplification of molecular chirality by circular polarized light, *Science* **273**, 1686 (1996).
- [36] D. R. Link, G. Natale, R. Shao, J. E. MacLennan, N. A. Clark, E. Korblova, and D. M. Walba, Spontaneous formation of macroscopic chiral domains in a fluid smectic phase of achiral molecules, *Science* **278**, 1924 (1997).
- [37] P. Kumari, B. Basnet, M. O. Lavrentovich, and O. D. Lavrentovich, Chiral ground states of ferroelectric liquid crystals, *Science* **383**, 1364 (2024).
- [38] J. Seidel, L. W. Martin, Q. He, Q. Zhan, Y.-H. Chu, A. Rother, M. Hawkrigde, P. Maksymovych, P. Yu, M. Gajek, *et al.*, Conduction at domain walls in oxide multiferroics, *Nature materials* **8**, 229 (2009).

- [39] J. A. Mundy, J. Schaab, Y. Kumagai, A. Cano, M. Stengel, I. P. Krug, D. Gottlob, H. Doğanay, M. E. Holtz, R. Held, *et al.*, Functional electronic inversion layers at ferroelectric domain walls, *Nature materials* **16**, 622 (2017).
- [40] S. Farokhipoor, C. Magén, S. Venkatesan, J. Íñiguez, C. J. Daumont, D. Rubi, E. Snoeck, M. Mostovoy, C. De Graaf, A. Müller, *et al.*, Artificial chemical and magnetic structure at the domain walls of an epitaxial oxide, *Nature* **515**, 379 (2014).
- [41] J. Ma, J. Ma, Q. Zhang, R. Peng, J. Wang, C. Liu, M. Wang, N. Li, M. Chen, X. Cheng, *et al.*, Controllable conductive readout in self-assembled, topologically confined ferroelectric domain walls, *Nature nanotechnology* **13**, 947 (2018).
- [42] A. A. Belik, Y. Matsushita, and D. D. Khalyavin, Reentrant structural transitions and collapse of charge and orbital orders in quadruple perovskites, *Angewandte Chemie International Edition* **56**, 10423 (2017).
- [43] A. A. Belik, Y. Matsushita, M. Tanaka, R. D. Johnson, and D. D. Khalyavin, A plethora of structural transitions, distortions and modulations in Cu-doped BiMn<sub>7</sub>O<sub>12</sub> quadruple perovskites, *Journal of Materials Chemistry C* **9**, 10232 (2021).